Complex Fluid Dynamics in BioMEMS Devices: Modeling of Microfabricated Microneedles

D. Trebotich[1,2], J. D. Zahn[2,3] and D. Liepmann[1,2,3]
[1]Department of Mechanical Engineering, University of California, Berkeley, USA
[2]Berkeley Sensor and Actuator Center, Berkeley, CA, USA
[3]Department of Bioengineering, University of California, Berkeley, USA

ABSTRACT

MEMS technologies promises to revolutionize health care by providing precise control of biological fluids for both diagnoses and treatments. For example, microneedles can be used for sample collection for biological analysis, delivery of cell or cellular extract based vaccines, and sample handling providing interconnection between the microscopic and macroscopic world. Microneedles may be used for low flow rate continuous drug delivery such as the continuous delivery of insulin to a diabetic patient. Microneedles are interesting from a design perspective not only because of their small size but because they provide a range of geometries and flow characteristics. This paper uses microneedle design as an example of the potential interaction between experiment and computation for the improved design of microfabricated microfluidic devices in general.

Previously, fluid flow in microneedles was studied experimentally [1]. Here, we use computational modeling capabilities in concert with experimental results to optimize the design of medical microneedles and, thus, to shorten the whole design/fabrication cycle. We compare CFD simulations to analysis and experiments for flows in three microneedle geometries—straight, bent and filtered (Fig. 1). The bent microneedle was found to have the highest fluid carrying capacity of 0.082 ml/sec at 138 kPa with a Reynolds number of 738. A microneedle with a built in microfilter 192 μm wide, 110 μm high and 7 mm long also had flow rates of 0.07 ml/sec (Fig. 2). Although the throughput of these microneedles is low they still compare favorably with other microneedle designs. Laminar flow models were found to accurately predict the flow behavior through the microneedles. All computational modeling was performed with the CFDRC CFD-ACE+ suite of software tools.

	Bent Needle	Straight Needle	Filter Needle (before/after exp.)
Length (μm)	5500	5000	5000/1000
Width (μm)	160	80	80/1350
Height (μm)	80	80	60/60
Hydraulic Diameter (μm)	107	80	60/68.6

Figure 1. Needle parameters.

Needle Type	Number of Tests	Avg. Exp. Flow Rate (ml/s)	Anal. Flow Rate (ml/s)	Error (%)	Reynolds Number
Bent	4	.082± 0.004	0.088	7.3	738
Reinforced	9	0.040± 0.004	0.040	0.0	503
Filter	2	0.070± 0.01	0.083	17.9	688
Double Channel	1	0.032	0.034	6.2	260

Figure 2. Experimental versus analytical flow rates at a constant pressure head of 138 kPa.

ANALYSIS

For fully-developed, laminar flow the x-directed velocity profile in a rectangular duct with y and z cross section is given by [2,5]

$$v_x = \frac{16a^2}{\mu\pi^3}\left(-\frac{dP}{dx}\right)\sum_{i=1,3,5\ldots}^{\infty}(-1)^{(i-1)/2}\left[1-\frac{\cosh(i\pi z/2a)}{\cosh(i\pi b/2a)}\right]\frac{\cos(i\pi y/2a)}{i^3}$$
$$-a \le y \le a \qquad (1)$$
$$-b \le z \le b$$

where $2a$ is the length of one of the walls, and $2b$ is the length of the other wall. Integrating this profile across y and z gives the average flow rate, Q as

$$Q = \frac{4ba^3}{3\mu}\left(-\frac{dP}{dx}\right)\left[1-\frac{192a}{\pi^5 b}\sum_{i=1,3,5\ldots}^{\infty}\frac{\tanh(i\pi b/2a)}{i^5}\right] \qquad (2)$$

The average velocity, U, is $Q/(4ab)$. The pressure drop in the entrance region is estimated using the Blasius boundary layer solution over a flat plate [3,4,6]

$$\tau_s = \frac{0.332\mu U}{x}\sqrt{\mathrm{Re}_x} \qquad (3)$$

where x is the distance along the plate, τ_s is the plate shear stress, μ is the dynamic viscosity and Re_x is the Reynolds number based on the distance x. If it is assumed that a rectangular duct behaves as a collection of four plates then the pressure gradient can be estimated as

$$\frac{dP}{dx} = -\frac{4\tau_s}{D_h} \qquad (4)$$

and the entrance pressure drop is found by integrating

$$\Delta P_{ent} = \int_0^l \frac{4}{D_h}\tau_s dx = \frac{4(0.332)}{D_h}\sqrt{\rho\mu U^3}\int_0^l x^{-\frac{1}{2}}dx = \frac{8(0.332)}{D_h}\sqrt{\rho\mu U^3 l} \qquad (5)$$

where l is the entrance length or the needle length, whichever is shorter.

The entrance length is defined as the point where the pressure gradient was matched to that of the fully developed flow

$$\frac{dP}{dx} = -\frac{4\tau_s}{D_h} = \frac{-Q}{\frac{4ba^3}{3\mu}\left[1 - \frac{192a}{\pi^5 b}\sum_{i=1,3,5...}^{\infty}\frac{\tanh(i\pi b/2a)}{i^5}\right]} \quad (6)$$

It should be noted that this entrance length estimate is about 20% of the standard macroscopic empirical entrance length estimate of [4]

$$\frac{l}{D_h} = 0.59 + 0.055\,\mathrm{Re} \quad (7)$$

The entrance pressure drop is derived by make the simplifying assumption that the developing flow profile is a Blasius boundary layer and each wall in the flow channel is independent of each other, whereas the above equation is an empirical fit of measured data. Clearly the assumption made to derive the entrance pressure drop is not correct since each of the walls influence the fluid flow profile.

Next, the losses due to viscous drag on the walls of the needle and geometric effects are modeled by applying the Modified Bernoulli equation. The pressure drop across the needle is [4]

$$\Delta P = \Delta P_{ent} + \frac{1}{2}\rho\left(U_2^2 - U_1^2\right) + f\frac{L}{D_h}\frac{1}{2}\rho U^2 + K_{geom}\frac{1}{2}\rho U^2 \quad (8)$$

where L is the needle length minus the entrance length. The fraction factor, f, is

$$f = \frac{4|\Delta P_{dev}|}{\rho U^2}\frac{D_h}{L} \quad (9)$$

where ΔP_{dev} is the fully developed pressure drop. K_{geom} is the geometric loss factor, which for a bent needle is [4]

$$K_{geom} = 1.3 \quad (10)$$

while for a sudden contraction [4]

$$K_{geom} = \left(\frac{2}{m} - \frac{A_2}{A_1} - 1\right)^2 \quad (11)$$

where m is the root of the quadratic

$$\frac{1 - m\left(A_2/A_1\right)}{1 - \left(A_2/A_1\right)^2} = \left(\frac{m}{1.2}\right)^2 \quad (12)$$

and where A_1 and A_2 are the cross sectional areas before and after the contraction respectively.

RESULTS AND DISCUSSION

We have predicted pressure drop versus volumetric flow rate (flow resistance) for steady, incompressible viscous flow through the three microneedle geometries and then to compare to analytical and experimental results. All computations were performed using the CFD Research Corporation CFD-ACE+ suite of tools. The numerical grids were created by the GEOM module of CFD-ACE+ and are shown in Fig. 3. The steady flow equations for a viscous, incompressible fluid were solved using the ACE(U) solver. All data were post-processed in CFD-VIEW.

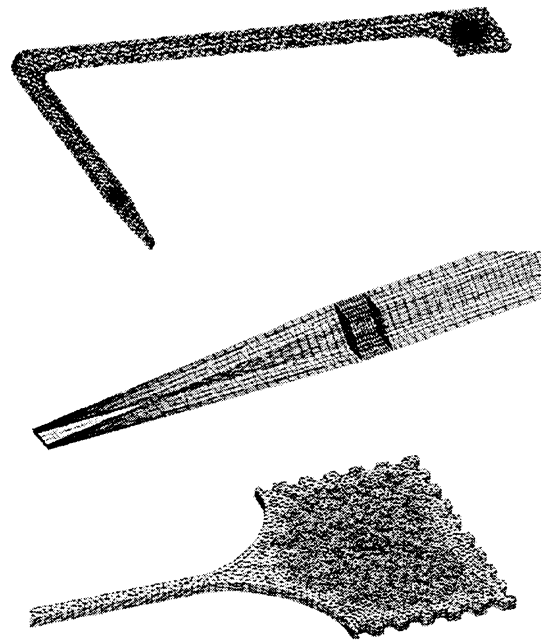

Figure 3: Unstructured grids for bent, straight and filter needles.

For a given flow rate, as determined by inlet conditions, the fluid pressure can be computed, (Fig. 4). As seen in Fig. 5, the computed pressure drops compare well to both the experimentally measured and analytically modeled pressure drops in the needles. Discrepancies between simulations and measurements may be attributed to losses due to the experimental equipment not modeled in the simulations, or processing variances which lead to slightly different flow channel dimensions than were simulated. However, all simulation and analytical results fall within the experimental error bars.

One point of interest is to understand the velocity profile in

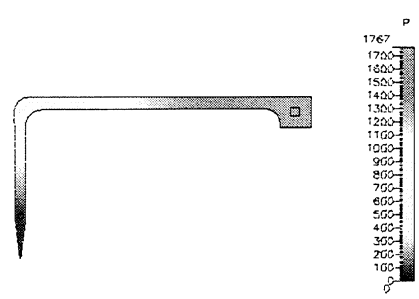

Figure 4: Representative pressure distribution from CFD simulation in bent needle. The flow rate was set to 150 μl/min.

the entrance region. When fluid enters a channel, it enters with a flat velocity profile (plug flow) and eventually evolves into the familiar parabolic flow profile. This transitional area is of importance since there is significant fluid drag on the sidewalls in the entrance region. The developing boundary layer has a sharper velocity gradient. Therefore, large molecules like proteins and DNA in a biological solution will see a strong extensional flow with a high wall shear upon entering a microneedle. The large forces on the molecules may be enough to induce cell lysis or shear induced chain excision of the proteins or DNA. Understanding of the development of the flow profile could lead to improved designs to limit wall shear stress to reduce shear-induced damage to biological molecules.

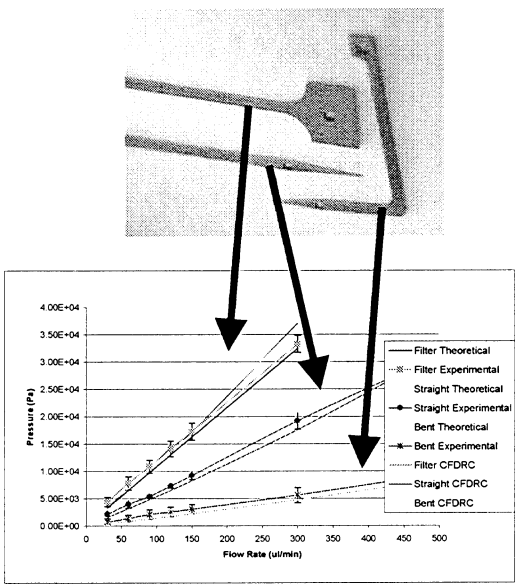

Figure 5. (Top) Needle geometries. (Bottom) Experimental, analytical and simulated flow resistances in different needle geometries.

As previously noted in the analysis, the entrance region was modeled as a collection of four independent plates over which a boundary layer was forming. This assumption is obviously incomplete, since the plates are not independent and the developing velocity profile is influenced by the four walls of the channel. In addition, the analysis used to obtain the pressure gradient (Eq. 6) assumes a constant free stream velocity which enters the channel tangent to the flow direction. In reality, since the needle inlet is perpendicular to the flow channel direction (needle lumen), fluid enters orthogonal to the flow channel; the free stream velocity in the direction of the flow channel is thus zero at the entrance (Fig. 6). And therefore, there is a gradient in the centerline velocity (extensional flow) not accounted for by the theory, which assumes a constant free stream velocity.

Fig. 7 shows the x-component of the centerline velocity in a straight needle as predicted by the CFD model. The cross sectional velocity near the entrance region is a much flatter

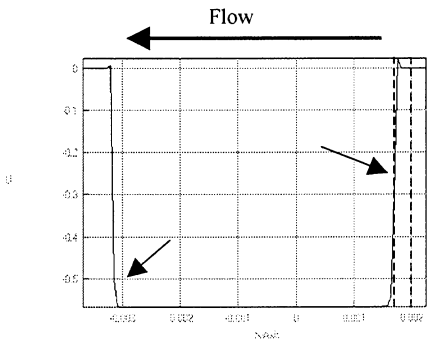

Figure 6: Centerline velocity profile in a straight needle at a flow rate of 120 μl/min.

profile than the fully developed flow profile. By looking at the centerline velocity the entrance length may be estimated. Since the fluid is entering normal to the flow passage the x-component of velocity is initially zero. The flow proceeds from right to left. The entrance length can be estimated as the distance down the needle lumen to reach the maximum centerline velocity. From observation, the entrance length in the simulations corresponds more closely to the standard empirically derived macroscopic entrance length (Eq. 7). This is not surprising since the analysis used to derive the analytical pressure gradient in the entrance region (Eq. 5) makes several simplifying assumptions. This region is also not responsible for a significant pressure loss when compared to the viscous losses in the fully developed flow through the rest of the needle.

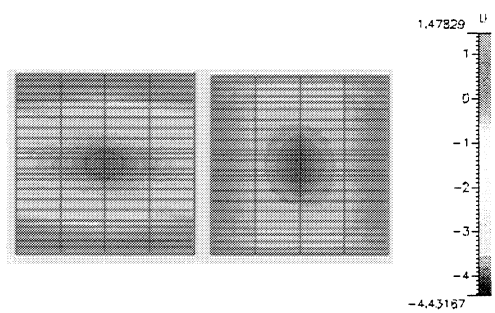

Figure 7: (Left) The x-directed velocity profile at the needle entrance. (Right) Fully developed x-directed velocity profile. (80 μm x 80 μm.)

The wall strain rate may also be computed as a function of distance down the needle (see Fig. 8). For a Newtonian fluid the wall shear stress is the strain rate times the fluid viscosity. The wall shear stress down the centerline of the needle in the entrance region is lower than the fully developed shear stress because the x-directed flow rate is initially zero. Therefore, the strain rate is initially lower, and gradually rises as the free stream velocity rises. However, in the corner of the needle the strain rate is much larger in the entrance region and thus drops off sharply; the fluid undergoes expansion to fill the whole channel volume upon entering the needle. It is important to see that for a Newtonian fluid the wall shear stress is over 300 Pa along

the centerline and over 200 Pa in the corner of the needle, which could lead to damage of cells or biological molecules in a solution. The strain rates would also be greater at higher flow rates.

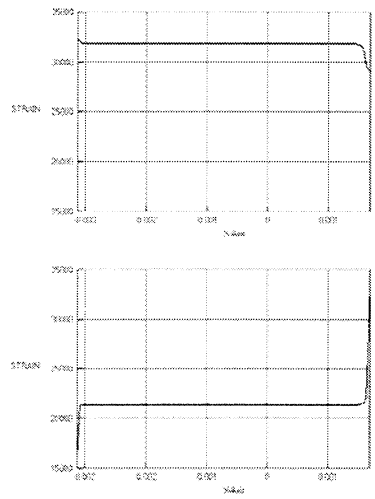

Figure 8. (Top) Strain rate along the wall of the microneedle down the centerline. Fluid entrance is at right and flow is to the left. (Bottom) Strain rate in the corner of the microneedle down the length of the needle. The fully developed strain rate is lower than the centerline. The flow rate is 120 μl/min.

Computational modeling also makes it possible to visualize the velocity field near complicated structures such as a bend, filter posts or sudden expansion (Fig. 9). We note that the largest error between theory and experiment occurred in the filter needles. This error is caused by the small spacing between the filter rungs. It can be shown that there is no boundary layer separation or recirculation around the bent needle. This is not surprising since the Reynolds number is

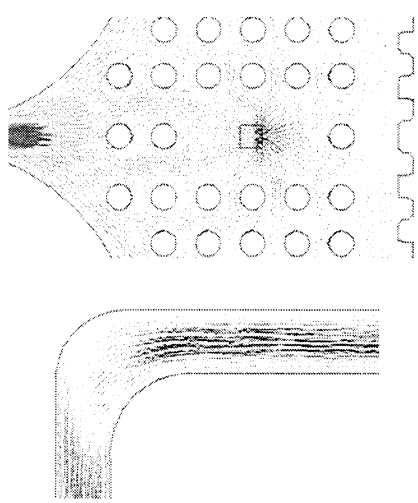

Figure 9: (Top) Flow around a bend in a microneedle. (Bottom) Flow after a sudden expansion in the filter microneedle.

less than 100 for all flows tested to obtain the experimental data for Figs. 1 and 5. However, the detailed flow structure near the expansion in the filter needle shows some interesting features. First, there is a viscous recirculation of fluid around the filter rungs. This validates the analytical assumption that the filter must be thought of as a combination of channels in series as well as in parallel. Also, the majority of the velocity field stays in the center of the flow channel and proceeds directly to the outlet after the expansion. The outlet acts as a sink which pulls the streamlines towards it. In conclusion, the filter is less important to the pressure drop than the lumen of the needle. However, a filter could be more effectively placed as a series of posts in a line to the outlet through which the majority of fluid flows, rather than evenly distributed throughout the needle head.

The computational models presented here agree well with experimental and analytical models. There are no real surprises for these flows which are viscous dominated and mainly two dimensional in the duct. However, analytical models break down in complex geometries and at the entrance. CFD lets us look at the velocity, pressure and strain distributions in these cases. This information feeds back into the design cycle for BioMEMS devices which in this case leads to improved microneedles but can clearly be expanded to other micro-fluidic devices.

ACKNOWLEDGMENT

This work was supported by the Defense Advanced Research Projects Agency's (DARPA) μFLUMES and Composite CAD programs.

REFERENCES

[1] J.D. Zahn, N.H. Talbot, D. Liepmann, A.P. Pisano, "Microfabricated Polysilicon Microneedles for Minimally Invasive Biomedical Devices," *Biomedical Microdevices*, 2:4 295-303, 2000.

[2] J.P. Brody, P. Yager, R.E. Goldstein and R.H. Austin, "Biotechnology at Low Reynolds Numbers," *Biophysical Journal*, **71**, pp. 3430-3441, Dec. 1996.

[3] L.G. Leah, "Laminar Flow and Convective Transport Processes. Scaling Principles and Asymptotic Analysis," Butterworth-Heinemann Series in Chemical Engineering, Boston, MA 1992.

[4] M.M. Denn, "Process Fluid Mechanics," Prentice Hall International Series in the Physical and Chemical Engineering Sciences.

[5] F.M White, "Viscous Fluid Flow, " second ed., McGraw-Hill Book Company, New York, NY, 1991.

[6] R.D. Blevins, "Applied fluid dynamics handbook," Krieger Publishing Company, Malabar, Florida, 1992.

[7] J.D. Zahn and D. Liepmann, "Complex Biological Fluid Flow Through Microfabricated Microneedles", Proceedings of the ASME IMECE MEMS 2000 Symposium, pp. 647-653, 2000.